DEPARTMENT OF THE INTERIOR

U.S. GEOLOGICAL SURVEY

STRENGTH MEASUREMENTS OF HEATED ILLITE GOUGE AT LOW AND HIGH PORE PRESSURES

by

D. E. Moore, R. Summers, and J. D. Byerlee[1]

Open-File Report 86-578

[1] U.S. Geological Survey, 345 Middlefield Road
Menlo Park, California 94025

1986

INTRODUCTION AND EXPERIMENTAL PROCEDURE

This report presents the stress-strain charts for a series of triaxial friction experiments on heated illite gouge. These results comprise the data set for Moore et al. (in preparation). Because of length considerations, only selected strength data are presented in that paper.

The experimental assembly, shown in Figure 1, is similar to other high-temperature designs for triaxial strength tests (e.g., Stesky et al., 1974; Lockner et al., 1982). The sample consisted of a layer of gouge 0.65 mm in thickness sandwiched between 30° finely ground sawcut surfaces in a granite cylinder 19.0 mm in diameter and 41.3 mm long. The gouge-filled cylinder was placed within an annealed copper jacket between titanium carbide end plugs and Lucalox insulators. The space between the copper-jacketed sample and the surrounding resistance heater was loosely packed with boron nitride, which is a good thermal and a poor electrical conductor.

Pore fluids were introduced to the sample along a central inlet that extended almost to the gouge layer by means of a hole drilled partway through the upper granite cylinder. The sawcut granite pieces were presaturated with deionized water to reduce the time required to equilibrate the pore fluid in the sample. Confining and pore pressures were applied first to the sample. Following that, the temperature was raised to the desired value and held there for 1800 s before the differential stress was applied. Temperatures were monitored by a thermocouple inserted along the pore pressure inlet. Pressures and strains were computer-controlled and -recorded; force and displacement measurements were made outside the pressure vessel.

The experiments conducted are summarized in Table 1. The experiments were run at temperatures of 200°, 400° and 600°C. Confining and pore pressures varied together, such that the effective pressure was kept constant at 100 MPa (99.9 MPa in the experiments at 0.1 MPa pore pressure). A few additional experiments were run at 0.1 MPa pore pressure and either 175 or 250 MPa confining pressure. The pore fluid was deionized water, and the maximum fluid pressure tested was 100 MPa. The experiments were run at strain rates of 10^{-4}/s and 10^{-6}/s, which correspond to average sliding velocities along the sawcut of 4.8 μm/s and 4.8 x 10^{-2} μm/s, respectively. These velocities refer to the average rate at which one granite piece slides past the other along the sawcut. For samples that show stick-slip, velocities within the gouge layer will differ significantly between the stick and slip portions of each cycle.

SUMMARY OF RESULTS AND THEIR SIGNIFICANCE

Stress-strain plots for the illite experiments in Table 1 are shown in Figures 2-14. The differential stresses supported by the gouge samples after 2 mm axial compression (or 2.3 mm slip along the sawcut) are plotted against the pore pressure for the experiments run at or near 100 MPa effective pressure in Figures 15-17. Also included in Figures 15-17 are results for the illite gouge at 3 MPa pore pressure and 100 MPa confining pressure, taken from Moore et al. (1983, 1986). The 97 MPa effective pressure of these additional runs is close to the 100 MPa effective pressure of the other experiments, and the strengths are also comparable. The results of these experiments are described briefly below; for additional discussion see Moore et al. (in preparation).

Frictional Strength

Several trends are apparent from these diagrams. The illite gouge shows a marked increase in strength with temperature increase; at 600°C, the gouge supports approximately three times the differential stress that it does at 200°C. The gouge also supports higher stresses at higher effective pressures (Figures 13-15). Increasing the pore pressure at a constant imposed effective pressure does not alter on the strength of the illite gouge at 200°C (Figure 15). There are also no velocity effects at 200°C. However, at 400°C (Figure 16) and 600°C (Figure 17), the strength decreases with increasing pore pressure, and the gouge shows somewhat different behavior at the two velocities. At 4.8 μm/s slip rate, the frictional strength of the gouge shows an immediate decrease with pore pressure increase, but at pore pressures above 60 MPa the strength levels off to about 225 MPa at 400°C and 280 MPa at 600°C. At 4.8 x 10^{-2} μm/s, the gouge strength is unaffected by pore pressure increase to about 30 MPa and then decreases somewhat irregularly at higher pore pressures.

The strength behavior is attributed to the compaction and welding of the gouge, which cause significant reductions in permeability and porosity. At low pore pressures, this lithification process leads to strength increases. At high pore pressures, large excess pore pressures are generated in the gouge layer during heating, owing to a combination of reduced pore space, clay-mineral dehydration, and high-temperature expansivity of the pore fluids. Because of the reduced permeability, the excess pressures are only slowly alleviated, thereby causing short-term strength reductions. The high-pore-pressure experiments at the slower velocity have in effect longer equilibration times, and their strengths are correspondingly higher.

Sliding Behavior and Correlation with Deformation Textures

The illite gouge shows a greater tendency to stick-slip movement at higher temperatures and at lower pore pressures, effective pressures, and sliding velocities. The average size of the stress drops was also higher at higher temperatures and lower velocities. A series of deformation styles (Figure 18) was identified in the gouge run products that can be correlated with the sliding behavior. At one extreme (texture a), the entire gouge layer shows deformation features, including kink bands and stretched grains. These run products do not contain any shear bands, however, and the samples all slid stably during the experiments. Moving from textures b to d in Figure 18, one sees the progressive localization of slip along a few shear bands that cross-cut the gouge layer (R1 shears) or that occur along the boundary with the granite cylinder (boundary shears). As the shear bands become more prominent, the remaining gouge layer shows fewer and fewer deformation effects. In texture d samples, the gouge outside the shear bands is completely undeformed. The samples containing well-developed shear bands showed stick-slip behavior when the angle that the R1 shears made with the boundary shears was also relatively high (above 10-14°). These textural differences suggest that inhomogeneous stress distributions combined with high-angle R1 shears are required for stick-slip motion. The concentration of slip along a few shear planes in the gouge layer creates the potential for large, localized stress build-ups if motion in these zones is impeded. The high R1 shear angles may provide the impediment by inhibiting the transfer of slip between the boundary and R1 shears.

The fracture patterns observed in natural fault zones (e.g., Wallace, 1973; Wallace and Roth, 1967; Sibson, 1986) are very similar to the shear band orientations observed in the experiments. Because of this, conditions

promoting stick-slip in the laboratory may be used to predict the location of earthquakes along fault zones. For sheet-silicate-rich gouges, relatively high temperatures, low displacement rates, and low confining and fluid pressures would promote instability of sliding.

Table 1. Experiments Conducted

Experiment	Temp. (°C)	Velocity (μm/s)	Pore Pr. (MPa)	Conf. Pr. (MPa)	Figure Numbers
1315	200	4.8	10	110	2,15
1314	200	4.8	20	120	3,15
1313	200	4.8	30	130	4,15
1379	200	4.8	40	140	5,15
1312	200	4.8	50	150	6,15
1376	200	4.8	60	160	7,15
1311	200	4.8	70	170	8,15
1377	200	4.8	80	180	9,15
1316	200	4.8	90	190	10,15
1378	200	4.8	100	200	11,15
1281	200	0.048	10	110	2,15
1282	200	0.048	15	115	15 only
1283	200	0.048	20	120	3,15
1329	200	0.048	30	130	4,15
1331	200	0.048	40	140	5,15
1328	200	0.048	50	150	6,15
1335	200	0.048	60	160	7,15
1327	200	0.048	70	170	8,15
1334	200	0.048	80	180	9,15
1319	200	0.048	90	190	10,15
1333	200	0.048	100	200	11,15
1362	400	4.8	10	110	2,16
1299	400	4.8	20	120	3,16
1300	400	4.8	30	130	4,16
1361	400	4.8	40	140	5,16
1301	400	4.8	50	150	6,16
1360	400	4.8	60	160	7,16
1302	400	4.8	70	170	8,16
1359	400	4.8	80	180	9,16
1303	400	4.8	90	190	10,16
1358	400	4.8	100	200	11,16
1280	400	0.048	10	110	2,16
1279	400	0.048	15	115	16 only
1278	400	0.048	20	120	3,16
1277	400	0.048	25	125	16 only
1276	400	0.048	30	130	4,16
1349	400	0.048	40	140	5,16
1284	400	0.048	50	150	6,16
1348	400	0.048	60	160	7,16
1285	400	0.048	70	170	8,16
1347	400	0.048	80	180	9,16
1287	400	0.048	90	190	10,16
1346	400	0.048	100	200	11,16

Experiment	Temp. (°C)	Velocity (μm/s)	Pore Pr. (MPa)	Conf. Pr. (MPa)	Figure Numbers
1317	600	4.8	10	110	2,17
1308	600	4.8	20	120	3,17
1307	600	4.8	30	130	4,17
1326	600	4.8	40	140	5,17
1306	600	4.8	50	150	6,17
1325	600	4.8	60	160	7,17
1310	600	4.8	70	170	8,17
1324	600	4.8	80	180	9,17
1304	600	4.8	90	190	10,17
1323	600	4.8	100	200	11,17
1267	600	0.048	10	110	2,17
1270	600	0.048	15	150	17 only
1269	600	0.048	20	120	3,17
1264	600	0.048	25	125	17 only
1263	600	0.048	30	130	4,17
1322	600	0.048	40	140	5,17
1290	600	0.048	50	150	6,17
1321	600	0.048	60	160	7,17
1289	600	0.048	70	170	8,17
1320	600	0.048	80	180	9,17
1318	600	0.048	90	190	10,17
1262	600	0.048	100	200	11,17
1291	200	4.8	0.1	100	12,15
1367	200	4.8	0.1	175	13 only
1294	200	4.8	0.1	250	14 only
1336	200	0.048	0.1	100	12,15
1363	400	4.8	0.1	100	12,16
1374	400	4.8	0.1	175	13 only
1297	400	4.8	0.1	250	14 only
1364	400	0.048	0.1	100	12,16
1293	600	4.8	0.1	100	12,17
1369	600	4.8	0.1	175	13 only
1296	600	4.8	0.1	250	14 only
1365	600	0.048	0.1	100	12,17

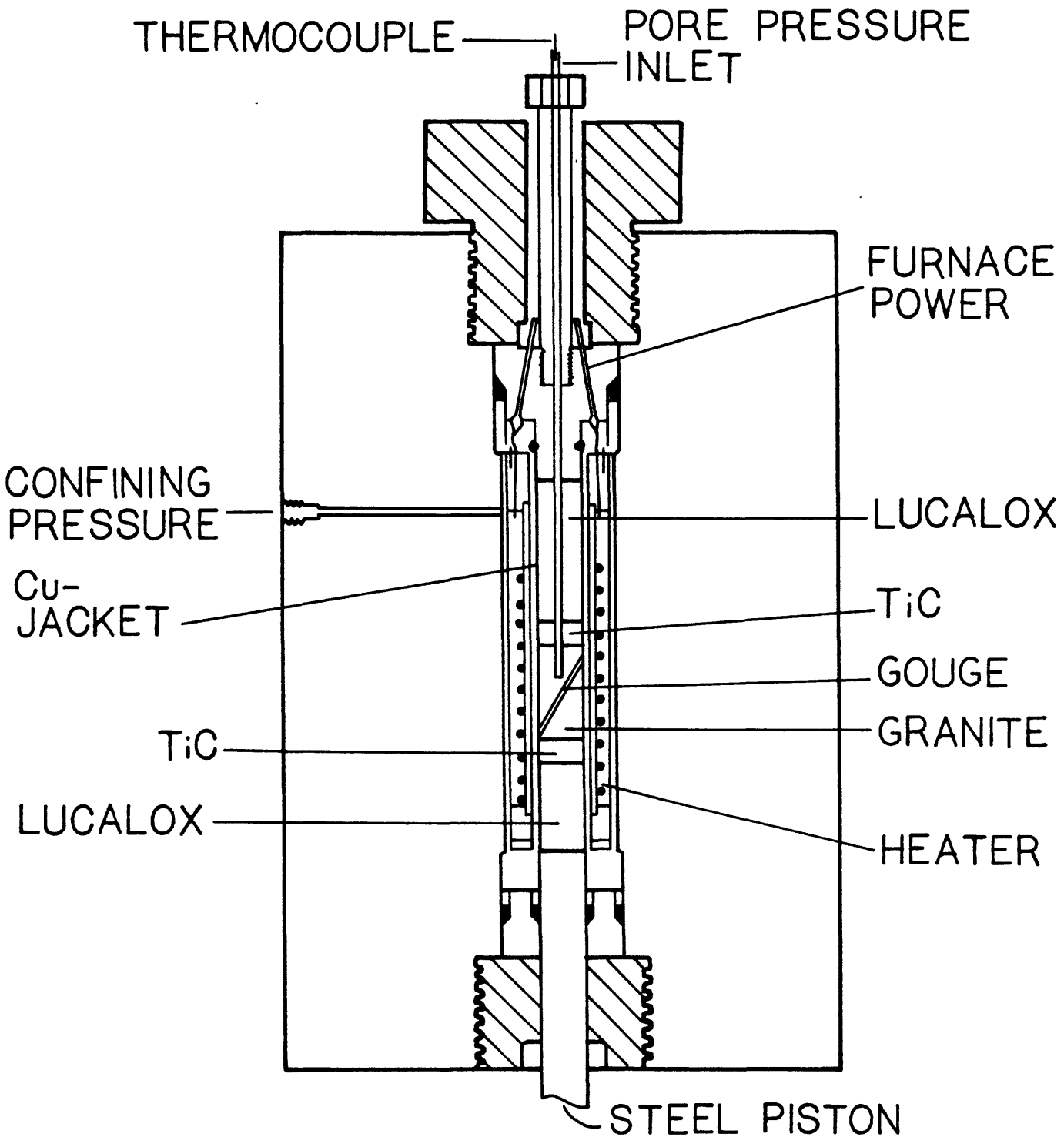

Figure 1. Experimental assembly.

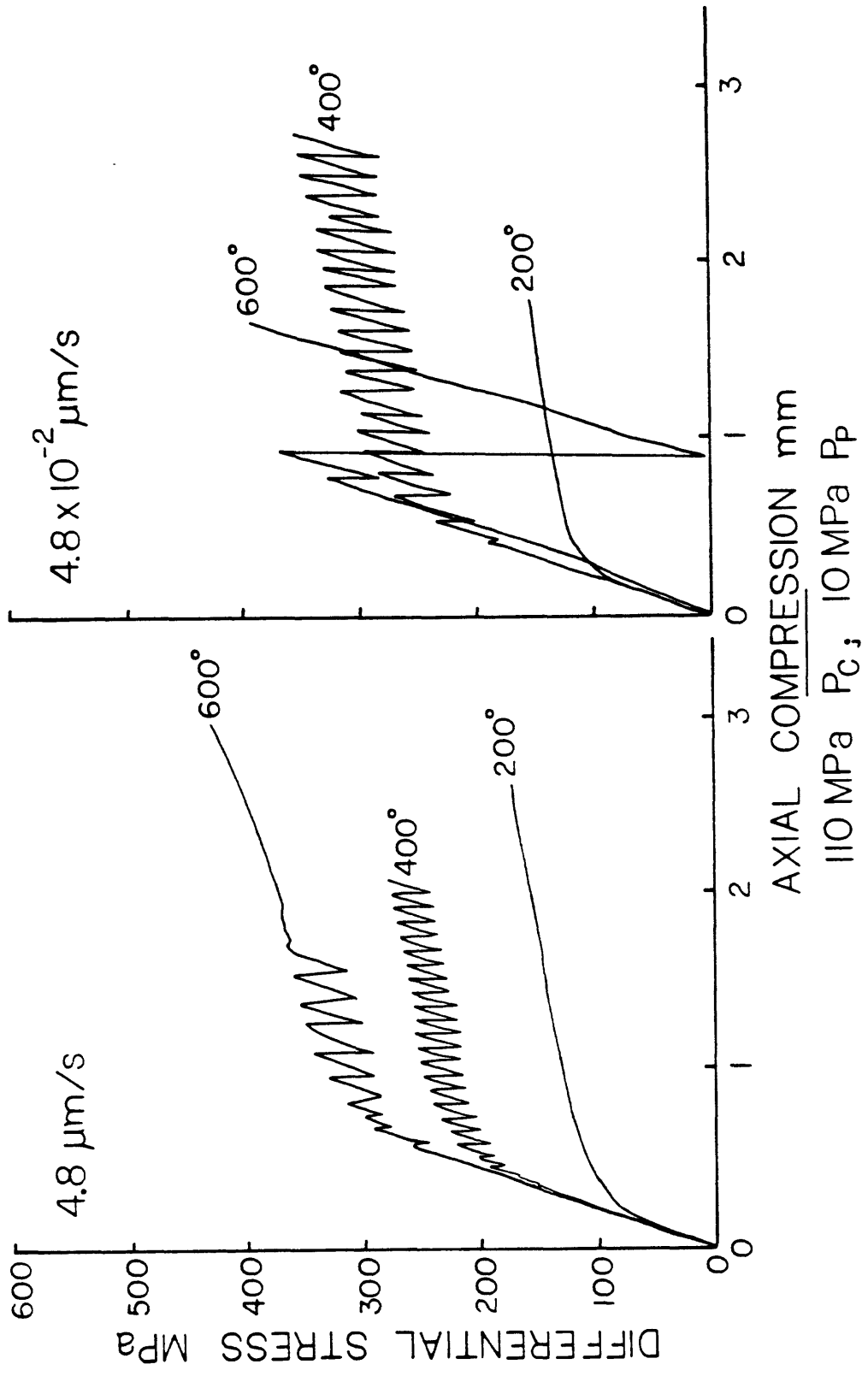
DIFFERENTIAL STRESS MPa
600
500
400
300
200
100
0
4.8 µm/s
600°
400°
200°
0
1
2
3
AXIAL COMPRESSION mm
110 MPa P_C; 10 MPa P_P
4.8 x 10^{-2} µm/s
600°
400°
200°
0
1
2
3

Figure 2.

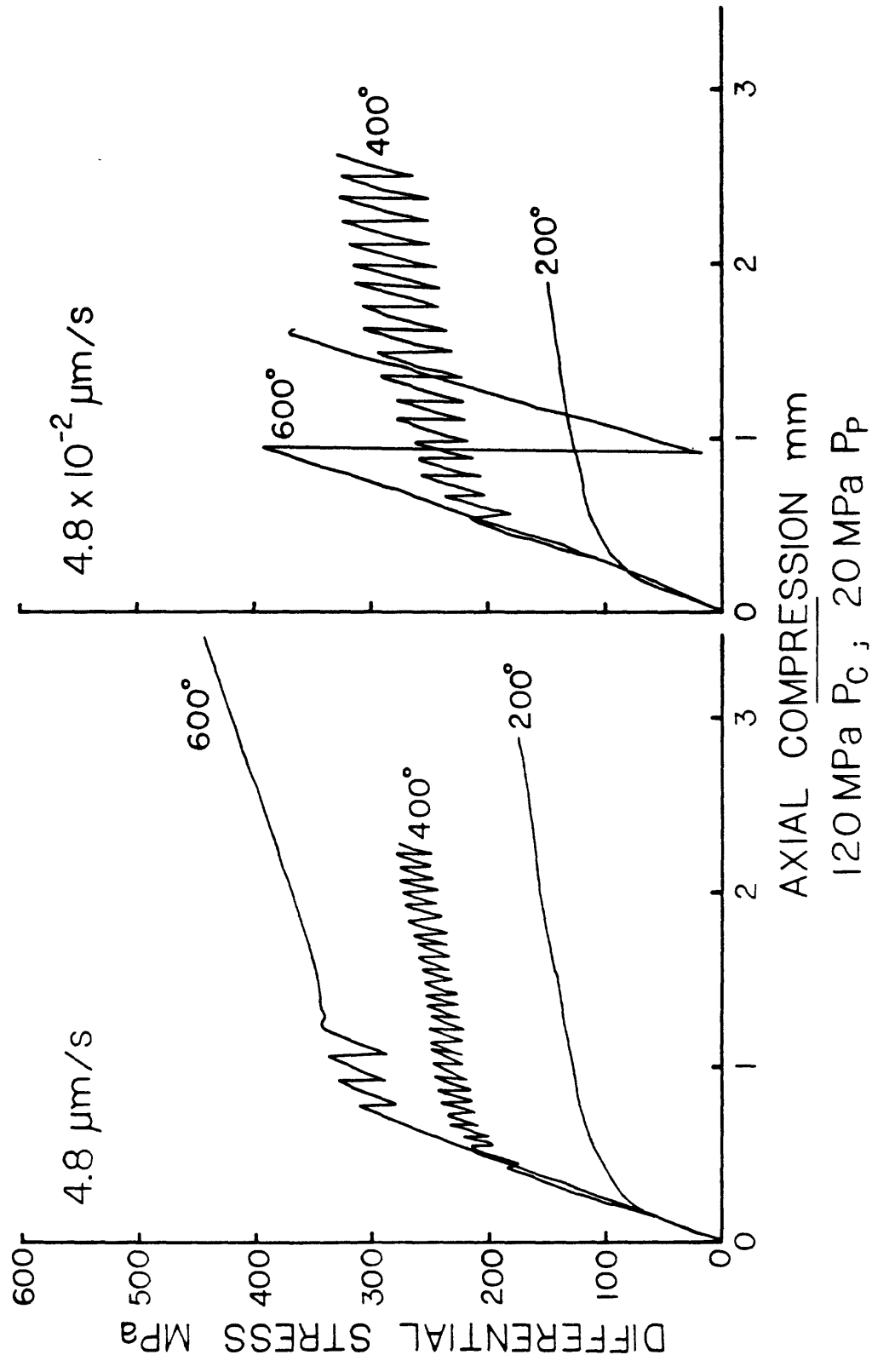
DIFFERENTIAL STRESS MPa
600
500
400
300
200
100
0
4.8 μm/s
600°
400°
200°
0
1
2
3
AXIAL COMPRESSION mm
120 MPa P_C ; 20 MPa P_P
4.8 x 10^{-2} μm/s
600°
400°
200°
0
1
2
3

Figure 3.

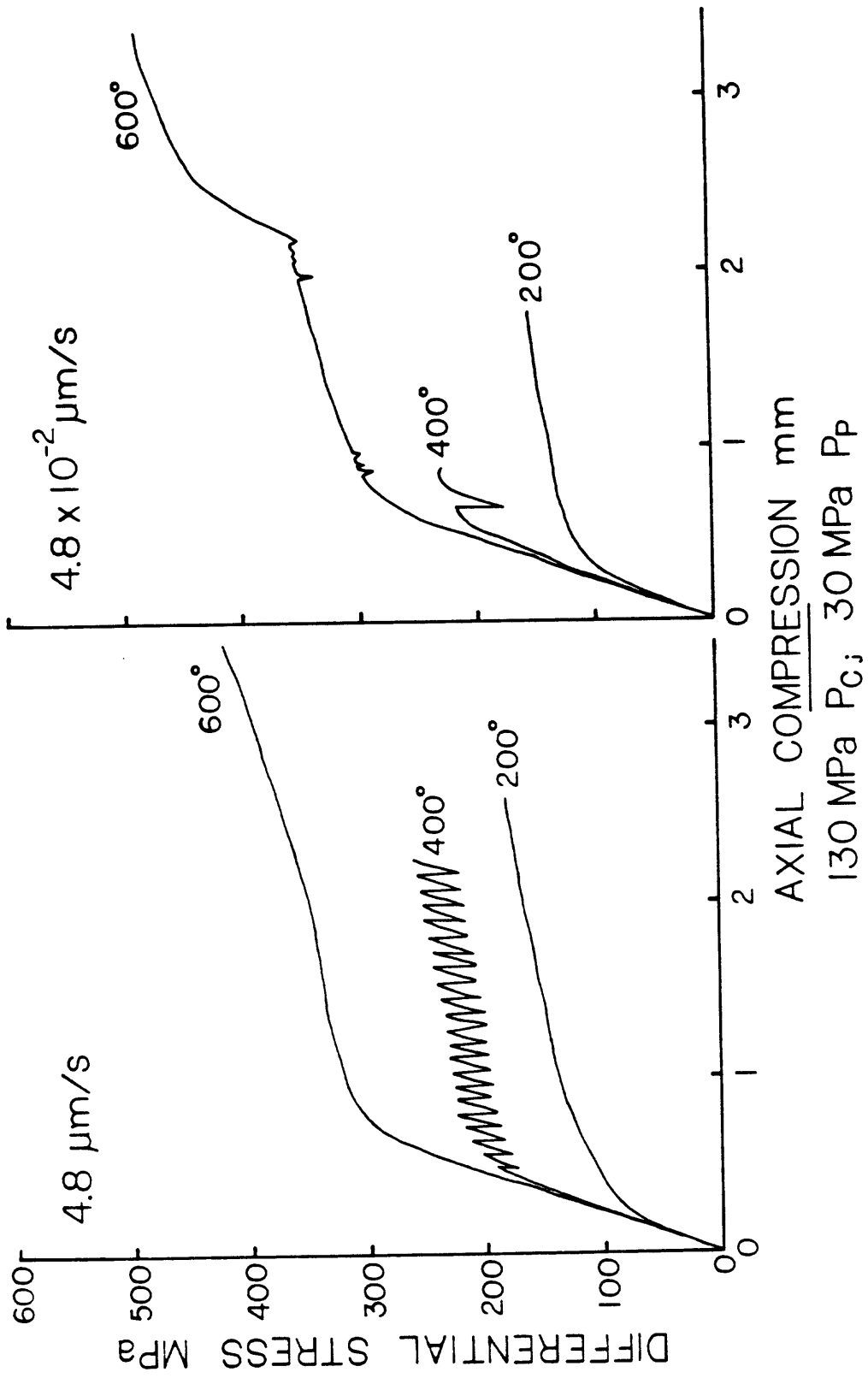
DIFFERENTIAL STRESS MPa
600
500
400
300
200
100
0
4.8 μm/s
600°
400°
200°
0
1
2
3
AXIAL COMPRESSION mm
130 MPa $P_{c;}$ 30 MPa P_P
4.8 x 10^{-2} μm/s
600°
400°
200°
0
1
2
3

Figure 4.

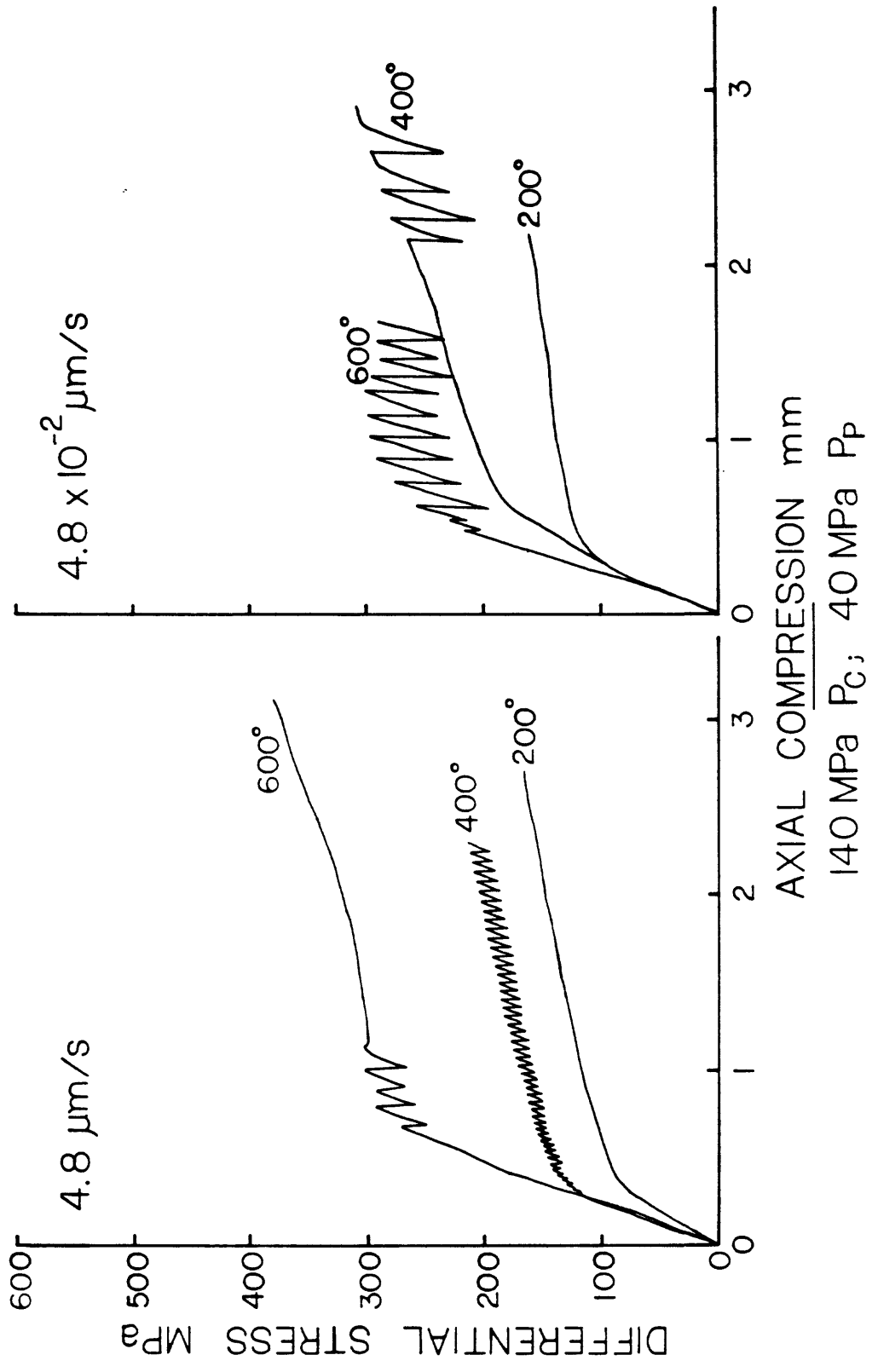
4.8 µm/s
4.8 x 10⁻² µm/s
600°
400°
200°
DIFFERENTIAL STRESS MPa
AXIAL COMPRESSION mm
140 MPa P_C; 40 MPa P_P

Figure 5.

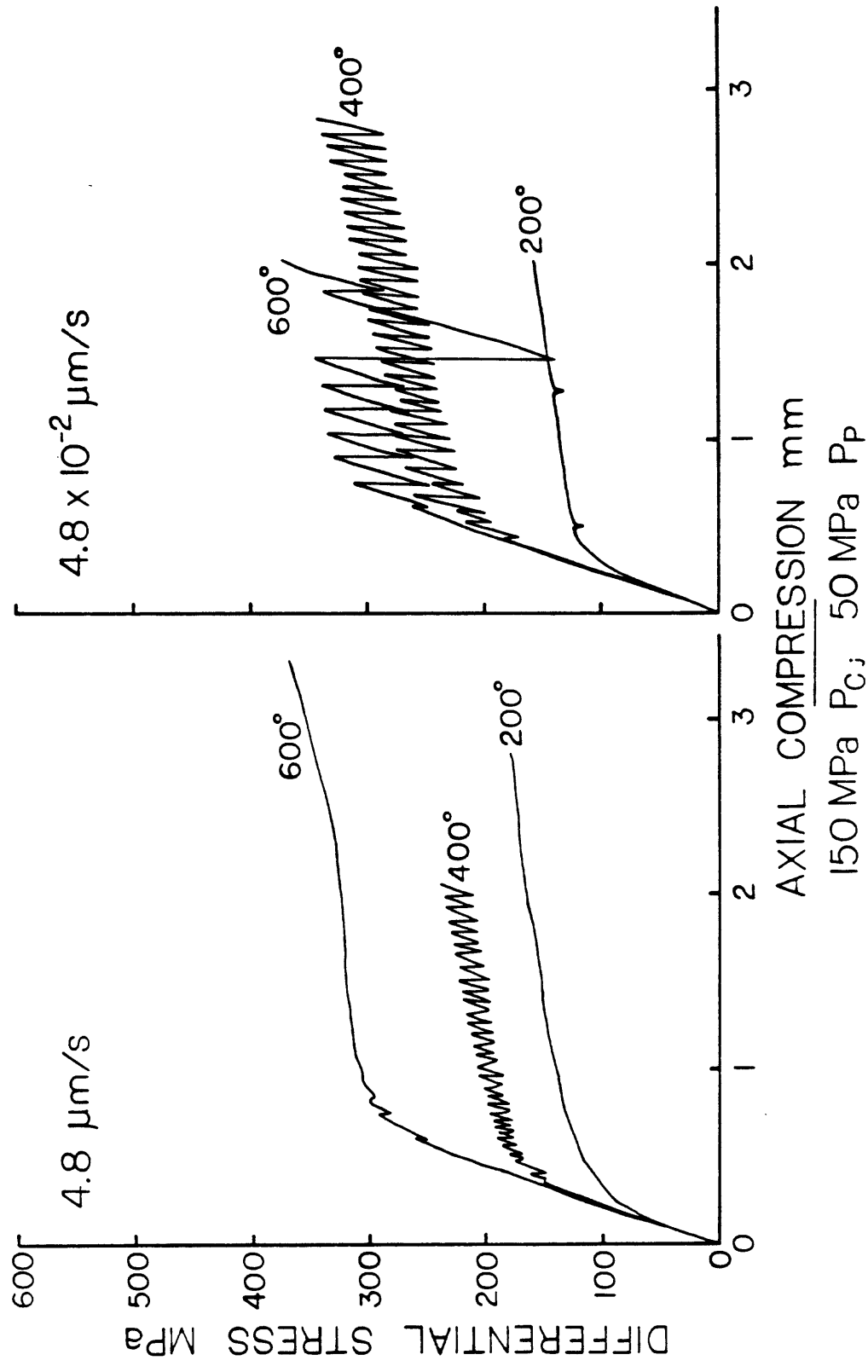
DIFFERENTIAL STRESS MPa
600
500
400
300
200
100
0
4.8 μm/s
600°
400°
200°
0
1
2
3
AXIAL COMPRESSION mm
150 MPa $P_{C;}$ 50 MPa P_P
4.8 x 10^{-2} μm/s
600°
400°
200°
0
1
2
3

Figure 6.

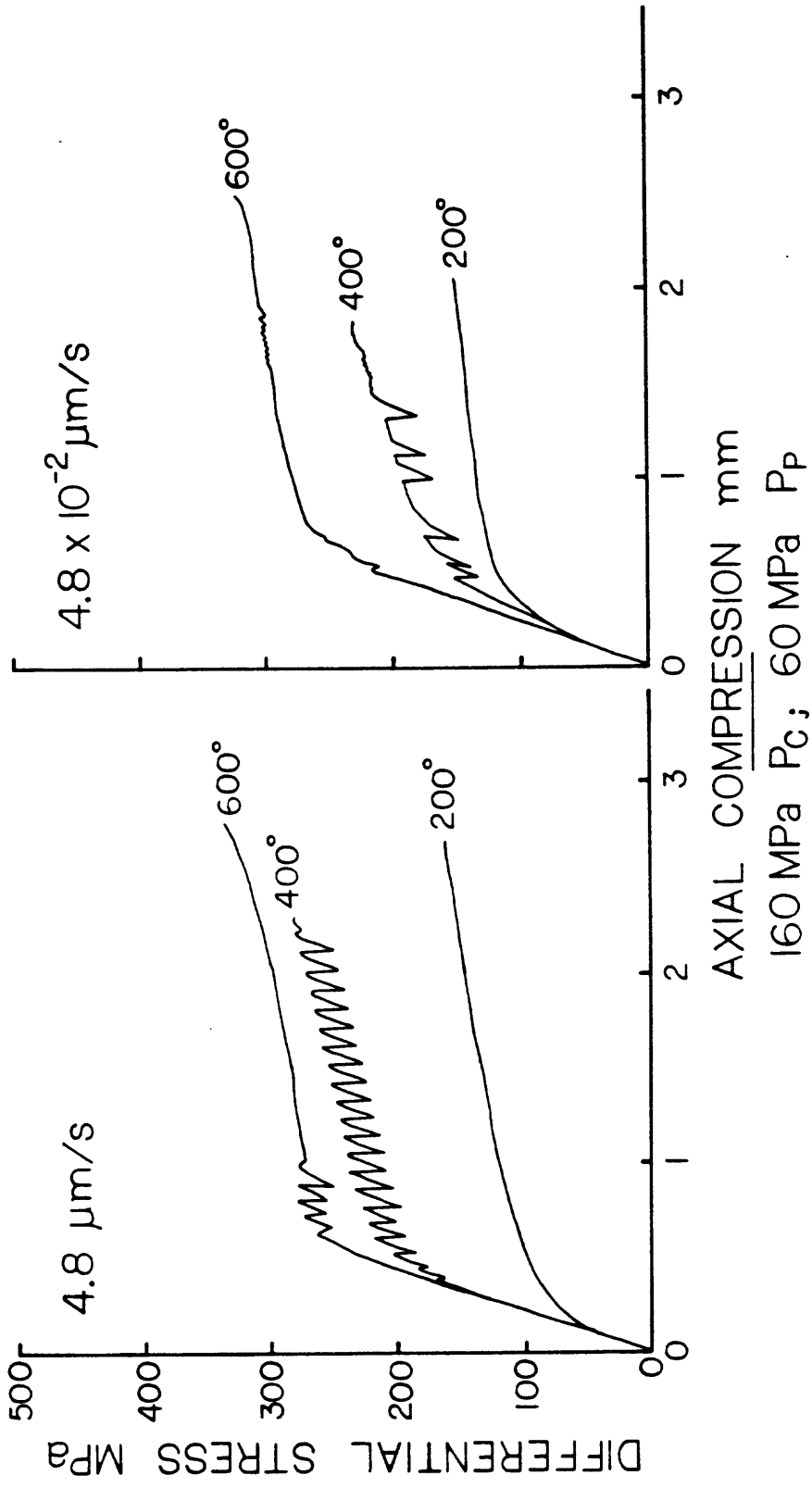
DIFFERENTIAL STRESS MPa
500
400
300
200
100
0
4.8 μm/s
600°
400°
200°
0
1
2
3
AXIAL COMPRESSION mm
160 MPa P_C; 60 MPa P_P
4.8 x 10^{-2} μm/s
600°
400°
200°
0
1
2
3

Figure 7.

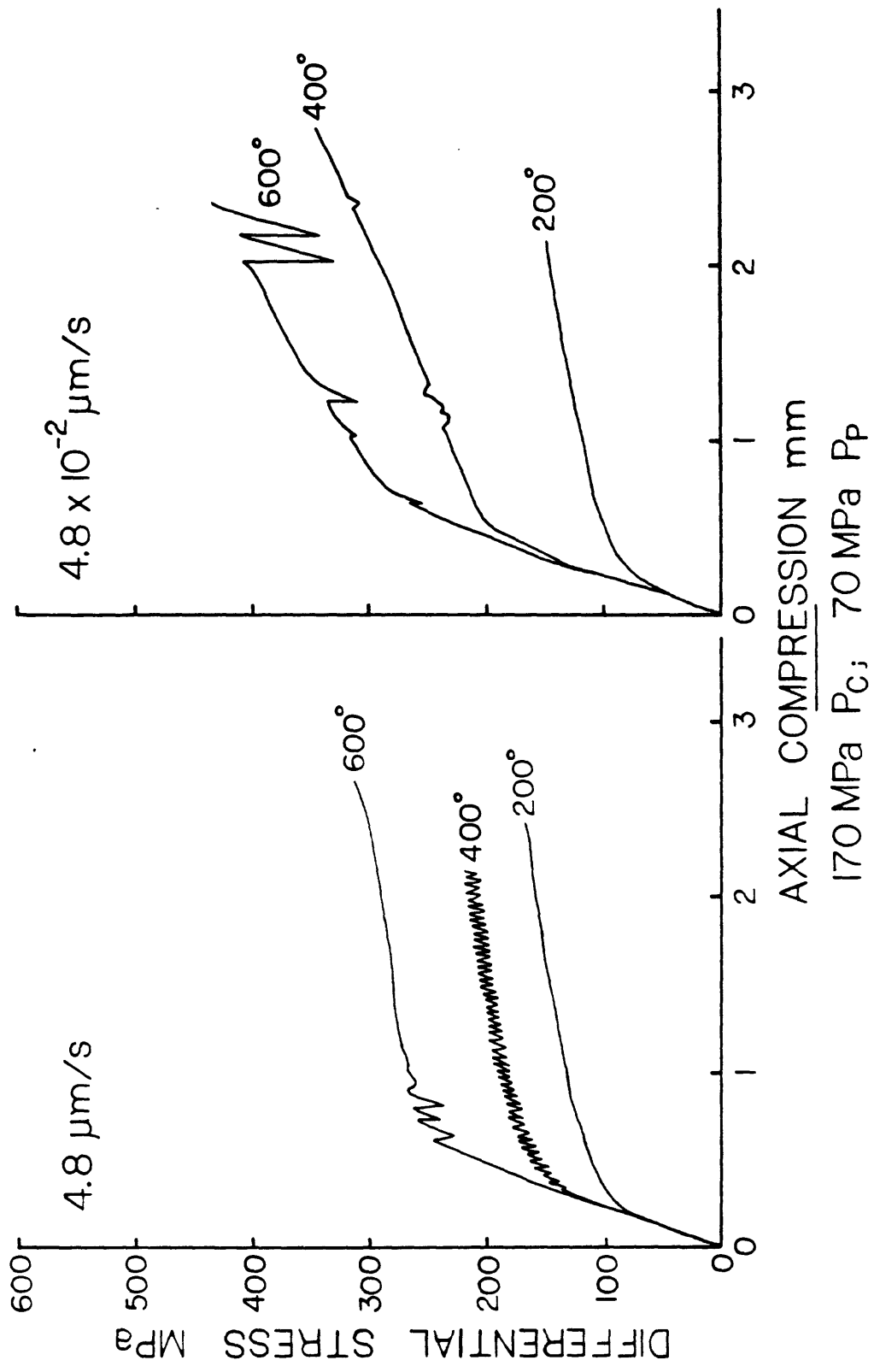
DIFFERENTIAL STRESS MPa
600
500
400
300
200
100
0
4.8 μm/s
600°
400°
200°
0
1
2
3
AXIAL COMPRESSION mm
170 MPa P_C; 70 MPa P_P
4.8 x 10^{-2} μm/s
600°
400°
200°
0
1
2
3

Figure 8.

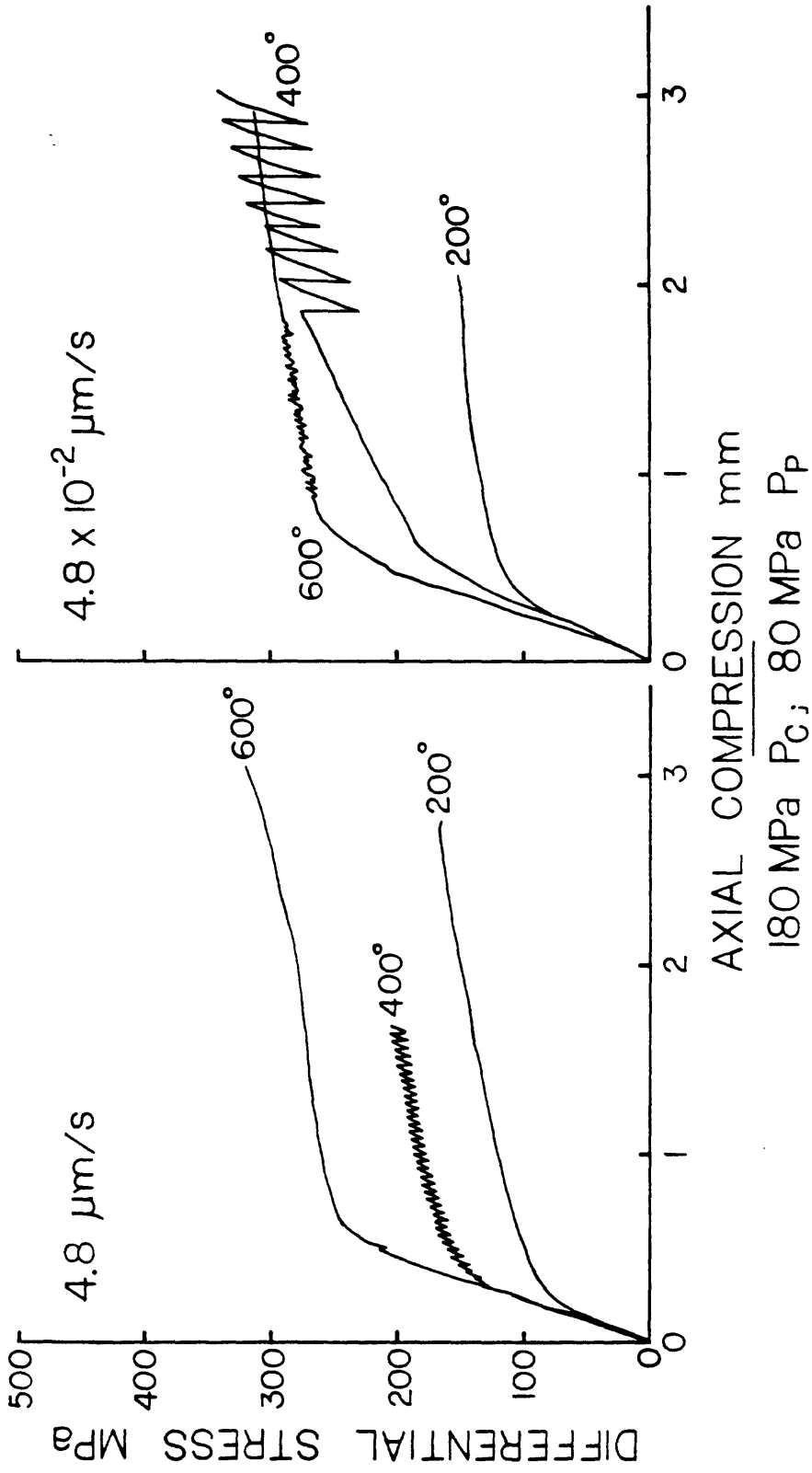
DIFFERENTIAL STRESS MPa
500
400
300
200
100
0
4.8 μm/s
600°
400°
200°
0
1
2
3
AXIAL COMPRESSION mm
180 MPa P_C; 80 MPa P_P
4.8 x 10^{-2} μm/s
600°
400°
200°
0
1
2
3

Figure 9.

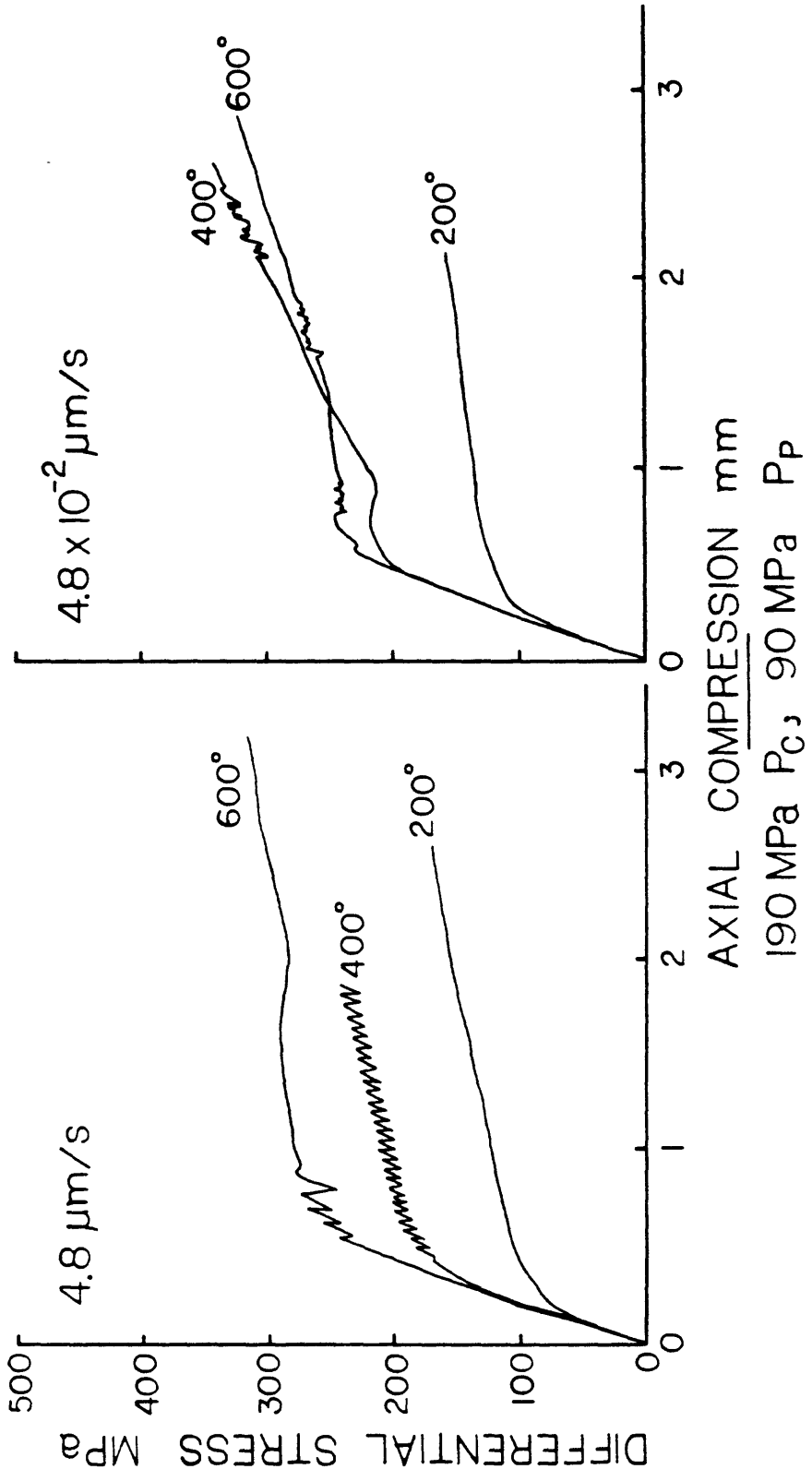
DIFFERENTIAL STRESS MPa
500
400
300
200
100
0
4.8 µm/s
600°
400°
200°
0
1
2
3
AXIAL COMPRESSION mm
190 MPa P_C, 90 MPa P_P
4.8 x 10^{-2} µm/s
600°
400°
200°
0
1
2
3

Figure 10.

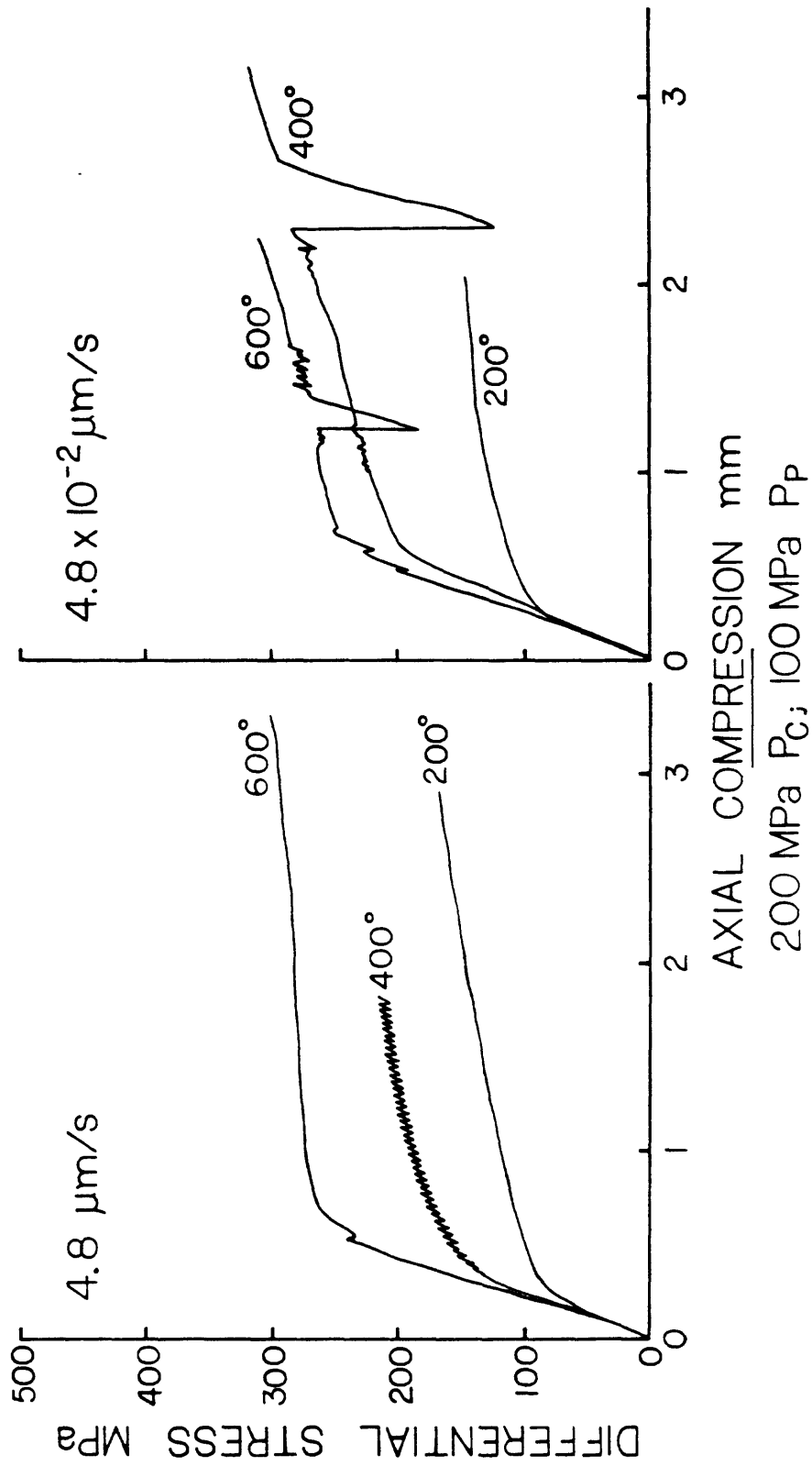
DIFFERENTIAL STRESS MPa
500
400
300
200
100
0
4.8 μm/s
600°
400°
200°
0
1
2
3
AXIAL COMPRESSION mm
200 MPa P_C; 100 MPa P_P
4.8 x 10^{-2} μm/s
600°
400°
200°
0
1
2
3

Figure 11.

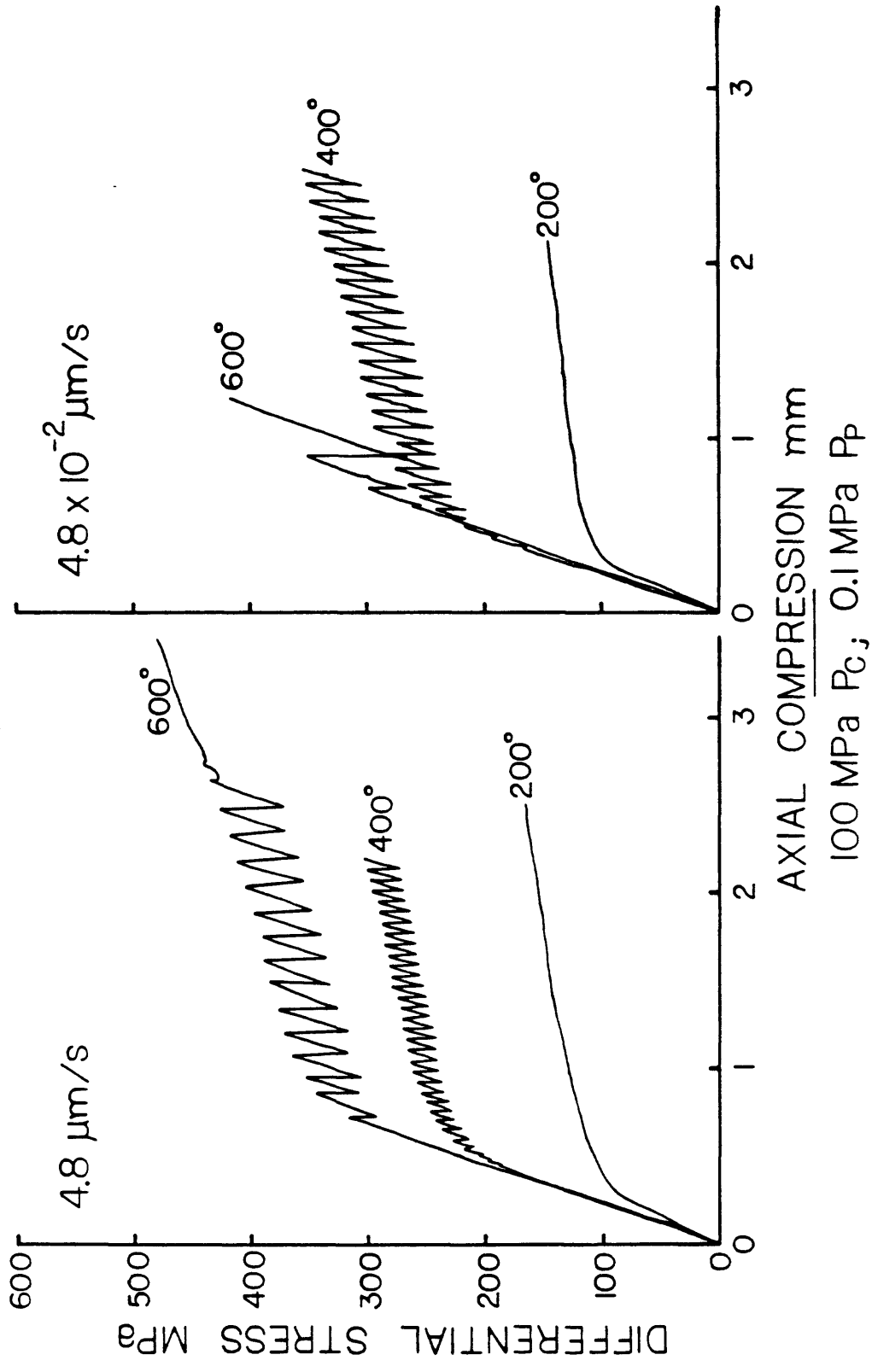
DIFFERENTIAL STRESS MPa
600
500
400
300
200
100
0
4.8 µm/s
600°
400°
200°
0
1
2
3
AXIAL COMPRESSION mm
100 MPa P_c; 0.1 MPa P_p
4.8 x 10^{-2} µm/s
600°
400°
200°
0
1
2
3

Figure 12.

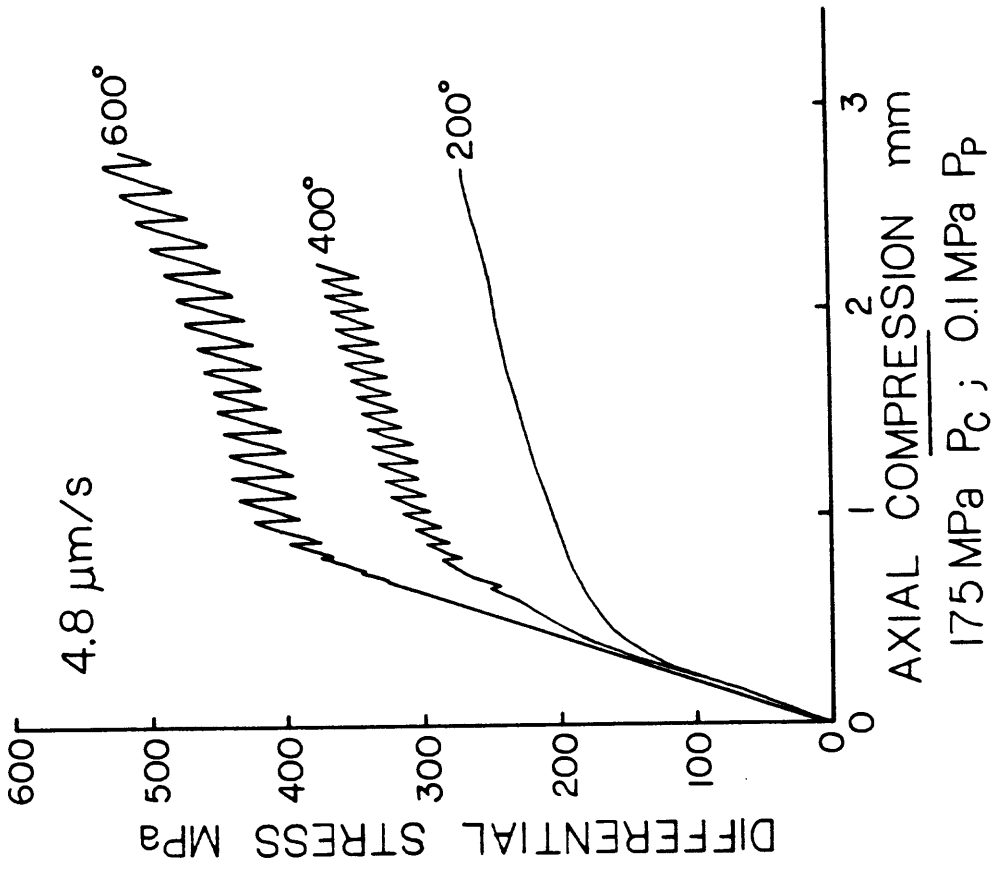
DIFFERENTIAL STRESS MPa
600
500
400
300
200
100
0
4.8 μm/s
600°
400°
200°
0
1
2
3
AXIAL COMPRESSION mm
175 MPa Pc ; 0.1 MPa Pp

Figure 13.

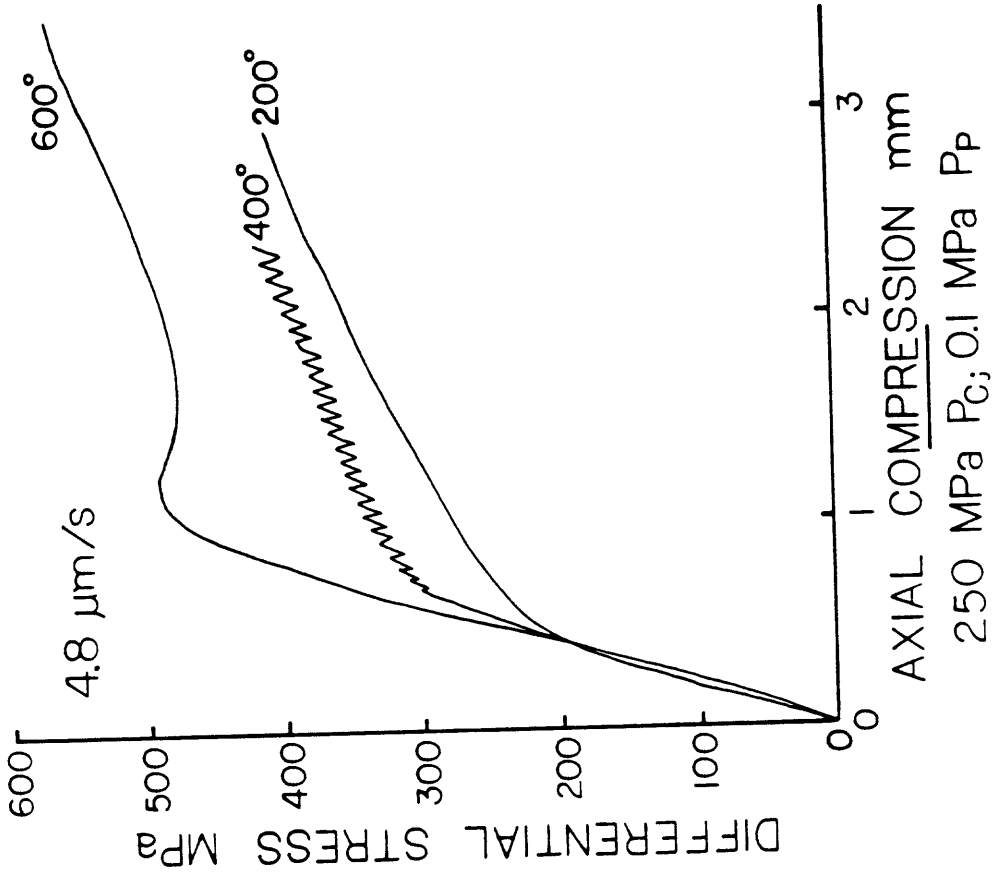
600°
400°
200°
4.8 µm/s
600
500
400
300
200
100
0
DIFFERENTIAL STRESS MPa
0
1
2
3
AXIAL COMPRESSION mm
250 MPa Pc; 0.1 MPa Pp

Figure 14.

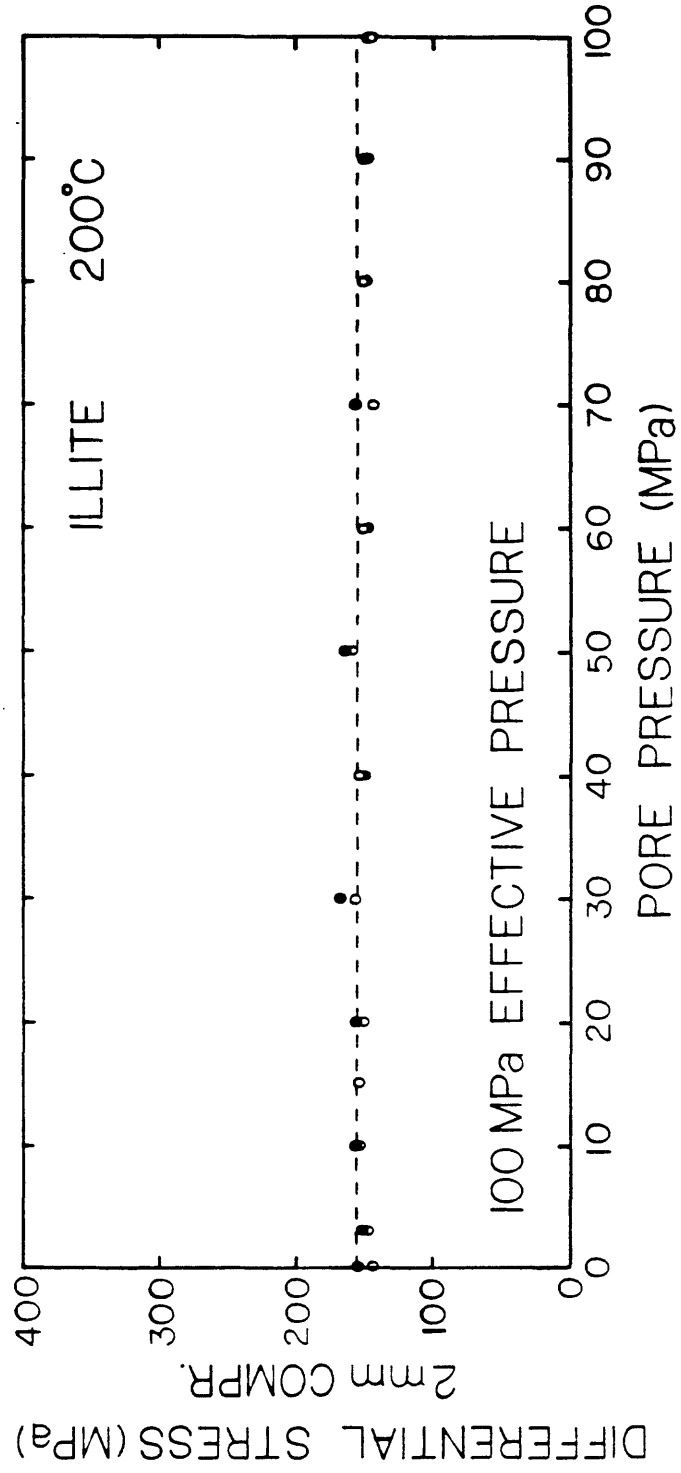

Figure 15. Differential stress after 2 mm axial compression (or 2.3 mm slip along the sawcut) for 200°C illite experiments. Also included are results at 3 MPa pore pressure and 100 MPa confining pressure from Moore et al. (1983, 1986). Open circles represent experiments run at 4.8×10^{-2} μm/s sliding velocity, and filled circles represent experiments at 4.8 μm/s. All the points lie close to a dashed line of constant differential stress, at approximately 160 MPa.

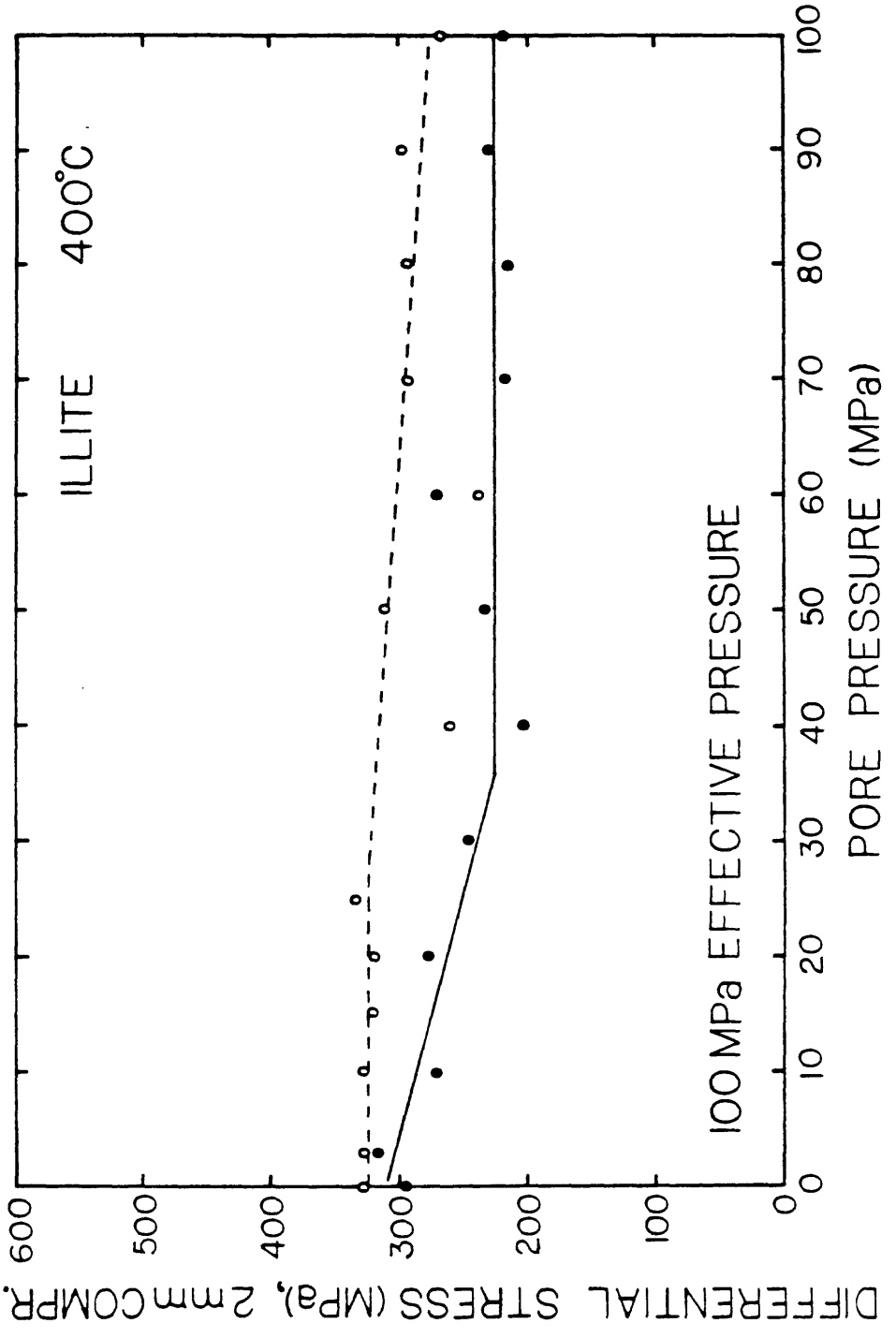

Figure 16. Differential stress after 2 mm axial compression (2.3 mm slip along sawcut) for 400°C illite experiments. Symbols as in Figure 15. Data at 3 MPa pore pressure are taken from Moore et al. (1983, 1986). The solid line connects most of the points for experiments at 4.8 μm/s slip rate, and the dashed line connects most of the points at 4.8×10^{-2} μm/s velocity. These lines show the general trends in strength at each velocity. A few of the points at both slip rates have relatively low strengths compared to the other results.

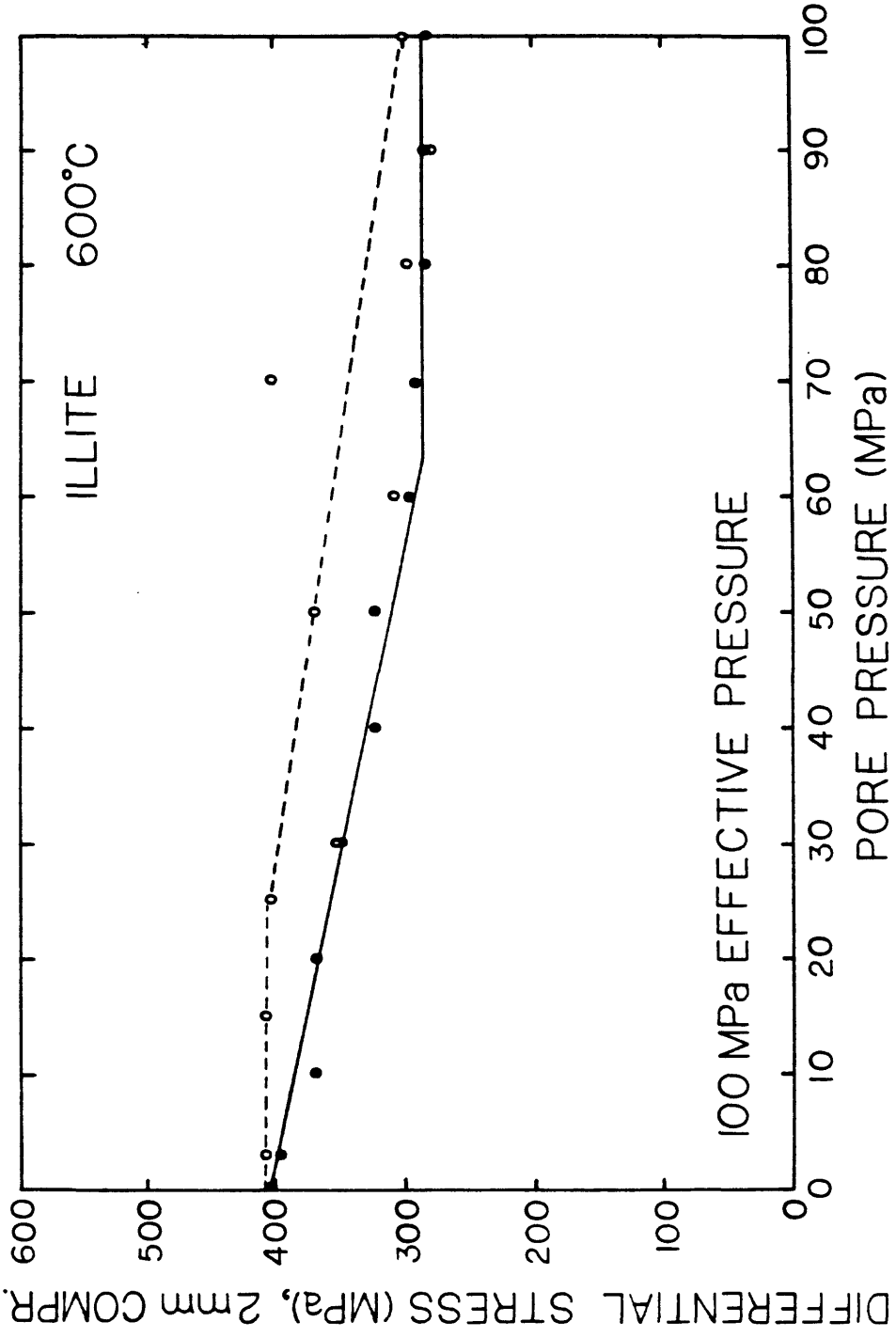

Figure 17. Differential stress after 2 mm axial compression (2.3 mm slip along sawcut) for illite gouge at 600°C. Symbols and lines as in Figures 15 and 16. Results at 3 MPa pore pressure from Moore et al. (1983, 1986). A few of the experiments at 4.8 x 10^{-2} μm/s have relatively low strengths compared to the other results, whereas the experiment at 70 MPa pore pressure has an unusually high strength that is comparable to the results at low pore pressures.

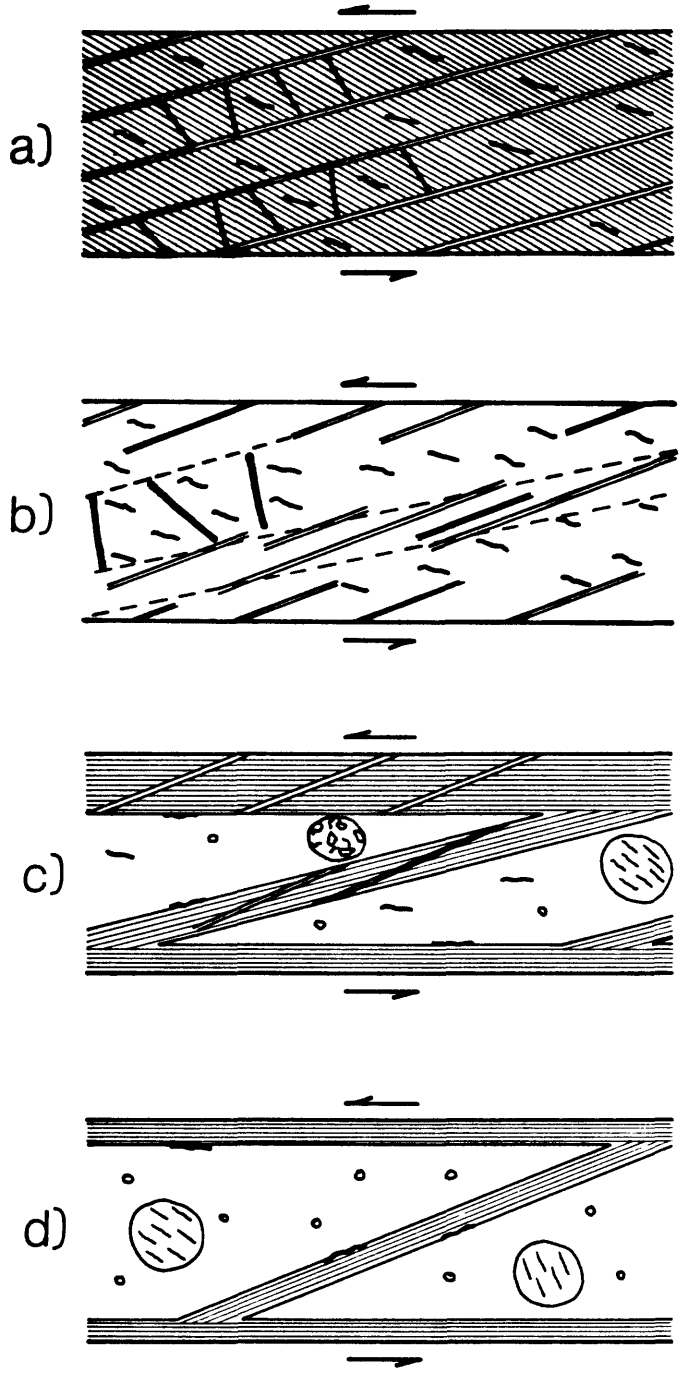

Figure 18. Textural classification of illite gouge run products.

REFERENCES

Lockner, D.A., Summers, R., Moore, D., and Byerlee, J.D., 1982. Laboratory measurements of reservoir rock from the Geysers geothermal field, California, International Journal of Rock Mechanics and Mining Sciences and Geomechanics Abstracts 19: 65-80.

Moore, D.E., Summers, R., and Byerlee, J.D., 1983. Strengths of clay and non-clay fault gouge at elevated temperatures and pressures, Proceedings 24th U.S. Symposium on Rock Mechanics: 489-500.

Moore, D.E., Summers, R., and Byerlee, J., 1986. The effect of sliding velocity on the frictional and physical properties of heated fault gouge, The Internal Structure of Fault Zones, C.-Y. Wang (ed.), Pure and Applied Geophysics Special Issue, in press.

Moore, D.E., Summers, R., and Byerlee, J.D., in preparation. Strength, sliding behavior, and deformation textures of heated illite gouge at low and high pore pressures.

Sibson, R.H., 1986. Earthquakes and lineament infrastructure. Phil. Trans. R. Soc. Lond. A317: 63-79.

Stesky, R.M., Brace, W.F., Riley, D.K., and Robin, P.-Y. F., 1974. Friction in faulted rock at high temperature and pressure, Tectonophysics 23: 177-203.

Wallace, R.E., 1973. Surface fracture patterns along the San Andreas fault. In: R.L. Kovach and A. Nur (editors), Proc. Conference on Tectonic Problems of the San Andreas Fault System. School of Earth Sci., Stanford Univ., Stanford, CA, Geol. Sci. XIII: 248-250.

Wallace, R.E., and Roth, E.F., 1967. Rates and patterns of progressive deformation. In: The Parkfield-Cholame California, Earthquakes of June-August 1966 -- Surface Geologic Effects, Water Resources Aspects, and Preliminary Seismic Data. U.S. Geol. Surv. Prof. Paper, 579: 23-40.